

Synthesis and electronic properties of transition metal oxide core-shell nanowires

Bo Lei, Song Han, Chao Li, Daihua Zhang, Zuqin Liu
and Chongwu Zhou¹

Department of Electrical Engineering, University of Southern California, Los Angeles,
CA 90089, USA

E-mail: chongwuz@usc.edu

Received 1 September 2006

Published 12 December 2006

Online at stacks.iop.org/Nano/18/044019

Abstract

This paper reviews our recent progress on the synthesis and transport studies of novel transition metal oxide nanowires, including $\text{YBa}_2\text{Cu}_3\text{O}_{6.66}$, Fe_3O_4 , $\text{La}_{0.67}\text{Sr}_{0.33}\text{MnO}_3$ and $\text{PbZr}_{0.58}\text{Ti}_{0.42}\text{O}_3$. Key to our success is the growth of standing single-crystalline MgO nanowires, which worked as excellent templates for epitaxial deposition of the desired transition metal oxides and led to high-quality core-shell nanowires. Transport studies have been conducted on both Fe_3O_4 and $\text{La}_{0.67}\text{Sr}_{0.33}\text{MnO}_3$ core-shell nanowires. Devices based on individual Fe_3O_4 nanowires exhibited room-temperature magnetoresistance of 1.2% under a magnetic field of $B = 1.8$ T, as a result of tunnelling of spin-polarized electrons across anti-phase boundaries. In addition, devices made of $\text{La}_{0.67}\text{Sr}_{0.33}\text{MnO}_3$ nanowires showed a remarkable metal-insulator transition at 325 K, accompanied by room-temperature colossal magnetoresistance (CMR) $\sim 10\%$ under a 1 T magnetic field. More interestingly, shape-induced magnetoresistance was also observed at room temperature with the $\text{La}_{0.67}\text{Sr}_{0.33}\text{MnO}_3$ nanowires. Our technique could enable various in-depth studies such as phase transition in nanoscale oxides and may pave the way for novel applications of these fascinating materials.

(Some figures in this article are in colour only in the electronic version)

One-dimensional nanostructures such as nanowires have stimulated enormous interest due to their significant promise as building blocks for functional materials, devices and systems. The past decade has witnessed tremendous progress towards the synthesis and applications of nanowires [1, 2]. A rich collection of these nanostructures was produced using various techniques including the vapour-liquid-solid (VLS) approach [3], solution-liquid-solid (SLS) method [4], solvothermal method [5] and template directed synthesis [6]. However, synthesis of one-dimensional (1D) transition metal oxides (TMOs) has been rarely reported due to their complex composition. As a result, only limited success has been achieved on a few materials, including $\text{BaTiO}_3/\text{SrTiO}_3$ nanorods [7], $\text{Co}_{0.05}\text{Ti}_{0.95}\text{O}_2$ nanotapes [8] and more recently

$(\text{La}, \text{Sr})\text{MnO}_3$ nanorods [9]. Recently, a great opportunity has been opened by a newly developed synthesis technique to produce a collection of TMO core-shell nanowires, including $\text{YBa}_2\text{Cu}_3\text{O}_{6.66}$ (YBCO), Fe_3O_4 , $\text{La}_{0.67}\text{Sr}_{0.33}\text{MnO}_3$ (LSMO), and $\text{PbZr}_{0.58}\text{Ti}_{0.42}\text{O}_3$ (PZT). These materials boast diverse and intriguing physical properties, including high T_c superconductivity for YBCO [10], spin polarization for Fe_3O_4 [11], colossal magnetoresistance for LSMO [12], and ferroelectricity for PZT [13]. In this approach, a pulsed laser deposition (PLD) method [14] was used to epitaxially deposit the desired TMO layer onto preformed MgO nanowire templates, thus forming core-shell nanowires. This novel technique yielded high-quality single-crystalline TMO nanowires and has rendered us a great opportunity to investigate their transport properties. Following the synthesis,

¹ Author to whom any correspondence should be addressed.

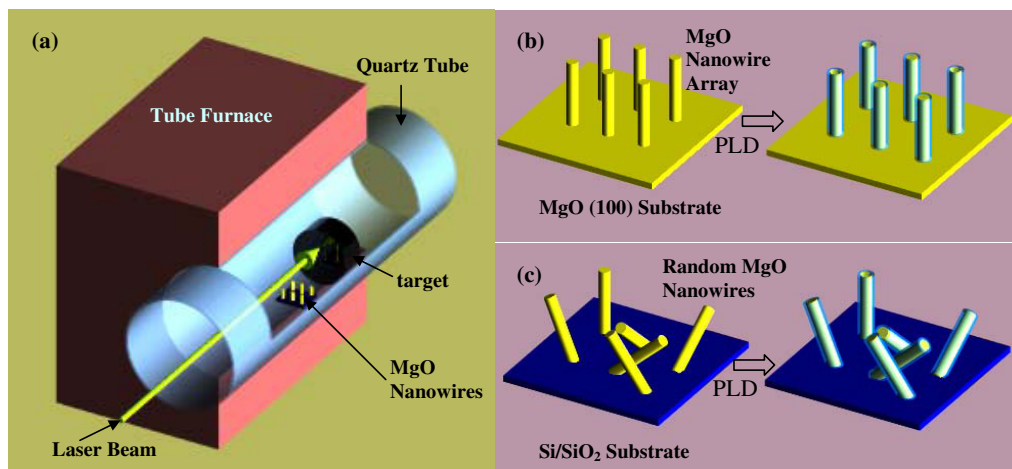


Figure 1. (a) Schematic drawing of the pulsed laser deposition system used for the transition metal oxide deposition. Schematic illustration of (b) vertically aligned MgO nanowire array on MgO (100) substrate and (c) randomly oriented MgO nanowires on Si/SiO₂ substrate before the PLD process and core-shell nanowires consisting of MgO nanowires coated with the desired material after the PLD process.

various characterization techniques have been utilized to confirm the morphology and material composition. Transport studies on Fe₃O₄ and LSMO nanowires have also been carried out, and intriguing magnetoresistance has been observed based on individual nanowires. This paper reviews our studies on various TMO core-shell nanowires.

The main process of our approach is illustrated in figure 1. We start with either vertically aligned or randomly oriented MgO nanowires grown on single-crystalline MgO(100) substrates (figure 1(b)) or Si/SiO₂ substrates (figure 1(c)) [15]. Armed with the MgO nanowire templates, the TMO shell layer can then be deposited using a PLD system consisting of a tube furnace and a Nd:YAG laser (figure 1(a)). The source target was prepared by compressing TMO powder followed by annealing. A frequency-doubled laser beam (532 nm) was directed to the target for ablation, with a repetition rate of 10 Hz. The MgO nanowire samples were positioned at a certain distance away from the target to collect the generated plume. Schematic illustrations of the standing MgO nanowires before and after the PLD process are shown in figures 1(b) and (c), showing a conformal coating of the desired material on the MgO nanowires. Below we discuss the synthesis and characterization of MgO nanowire templates and core-shell nanowires of various TMO materials.

We first developed a novel method to produce vertical arrays of single crystalline MgO nanowires following the vapour-liquid-solid mechanism [15]. Our system consists of a horizontal quartz tube furnace, which hosts a ceramic boat filled with Mg₃N₂ powder working as the feedstock. Single crystalline (100) MgO substrates coated with Au nanoclusters were put at the downstream of the Mg₃N₂ powder. The furnace was then heated to 900 °C with Ar mixed with a trace amount of oxygen flowing at 100 sccm all the time. After cooling, the MgO substrates appeared rough compared to the smooth surface before the growth. The as-grown product was then characterized by scanning electron microscopy (SEM), energy-dispersive x-ray spectroscopy (EDS), x-ray diffraction (XRD), transmission electron microscopy (TEM) and high-resolution TEM (HRTEM). We have prepared the gold nanoclusters using

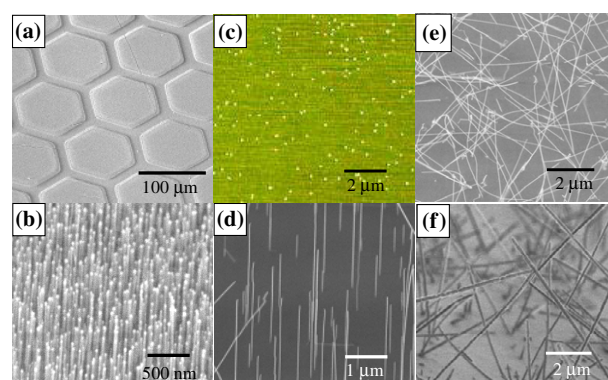


Figure 2. Synthesis of MgO nanowires by chemical vapour deposition. (a) Low-magnification SEM image of MgO nanowires grown on MgO(100) substrate. 1 nm gold film was evaporated through a TEM grid and used as the catalyst. (b) Higher magnification SEM image of the sample showing nanowires standing normal to the substrate. (c) AFM image of gold clusters before the growth on MgO(100) substrate. (d) SEM image of MgO nanowires grown with 30 nm gold clusters as catalyst. (e) Top view and (f) perspective view of randomly oriented MgO nanowires on a Si/SiO₂ substrate.

two methods. First, e-beam evaporation was used to coat the MgO substrates with 1 nm gold film, and a TEM grid was used as a shadow mask. Figure 2(a) depicts a low-magnification SEM image of the nanowires grown with the patterned Au film. MgO nanowires grew only within the hexagonal regions where Au films were deposited, indicating that gold worked as the catalyst. Figure 2(b) shows a high-magnification image of the same sample, and all the nanowires were observed to stand normal to the substrate with the gold catalytic particles showing at the tips as bright spots. These nanowires are typically several microns long and 30–100 nm in diameter. To gain further control over the nanowire diameter and also the array density, we also prepared MgO(100) substrates coated with monodispersed gold clusters of 30 nm in diameter (figure 2(c)), and a SEM image of the substrate after the MgO

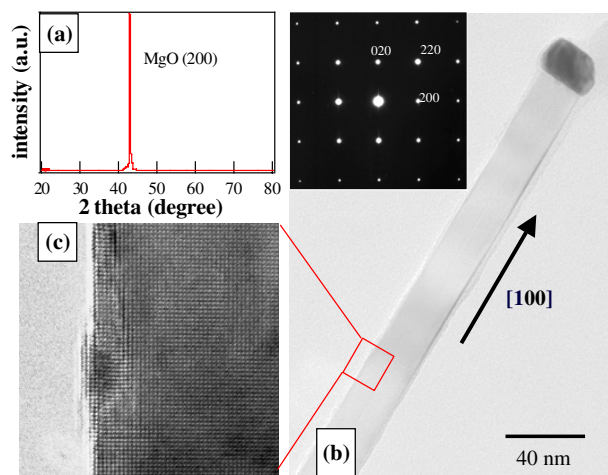


Figure 3. (a) XRD data of MgO nanowires grown on a MgO(100) substrate. (b) TEM image of an individual MgO nanowire. Inset is the nanowire diffraction pattern. The nanowire was identified to grow along the [100] direction. (c) HRTEM image showing the crystal lattice of the MgO nanowire.

nanowire growth is presented in figure 2(d). It clearly shows that these nanowires have uniform diameters and essentially all stand normal to the substrate. The density of nanowires is in good agreement with the density of catalysts. The length of the nanowires can be controlled by tuning the reaction time and a typical growth rate of $0.3\text{--}0.5\ \mu\text{m min}^{-1}$ was found for our synthesis.

We have also developed a highly efficient process to produce MgO nanowires with random orientations on Si/SiO₂ substrates, following the above-mentioned CVD method [16]. Figure 2(e) displays a top-view SEM image of the as-grown MgO nanowires. These nanowires follow random orientations, in sharp contrast to the vertically aligned MgO nanowires in figures 2(b) and (d). A perspective view (figure 2(f)) of the sample clearly reveals that the MgO nanowires are actually standing on the Si/SiO₂ substrate at various angles. These nanowires could therefore work as good templates for the subsequent PLD to produce the desired core-shell nanowires.

X-ray diffraction was carried out over vertically aligned MgO nanowire samples, and only one diffraction peak corresponding to MgO(200) plane was detected (figure 3(a)). This is a direct result of the epitaxial nature of the interface between our nanowires and the MgO substrates, and thus confirmed we obtained single-crystalline nanowires with [100] as the growth direction. This is further confirmed by detailed TEM analysis. Figure 3(b) shows the typical TEM image of the MgO nanowire, which is always found to be smooth, uniform and defect-free. Moreover, the nanowire terminates in a cluster similar in size to the nanowire diameter, indicating the MgO nanowire growth follows the catalyst-guided vapour-liquid-solid growth mechanism [15]. The lattice of the MgO nanowires can also be clearly seen in the HRTEM image shown in figure 3(c). The selected area electron diffraction (SAED) pattern of the MgO nanowire (figure 3(b), inset) reveals that the nearest diffraction spot to the centre corresponds to the (200) plane, which is the case for face-centred cubic crystal structures [17].

Similar to the conventional epitaxial film growth, these MgO nanowires [15, 16] provide a great opportunity to work as templates for other materials. Several advantages are worth mentioning for our MgO standing nanowires. The first is that these nanowires can be used to grow core-shell nanowires instead of nanotapes [8, 18]. These core-shell structures may exhibit intriguing physics, such as destruction of the global phase coherence in ultrathin superconducting cylinders [19], and may also work as building blocks for more sophisticated core-multishell structures. Secondly, MgO can work as the substrate for epitaxial growth of a wide variety of interesting materials, including YBCO, Fe₃O₄, LSMO and PZT, and thus a truly generic approach can be developed. These nanowires are very hard to grow using conventional chemical vapour deposition techniques due to their complex compositions and keen dependence on the temperature and pressure [20].

The developed PLD process is depicted in figure 1. The laser beam from a pulse mode Nd:YAG laser ($\lambda = 532\text{ nm}$) was focused onto a target and the generated plume was then deposited onto a substrate with standing MgO nanowires. The sample temperature, the ambient gas and the pressure were carefully tuned to optimize the epitaxial growth of the desired material on the MgO nanowires. One significant advantage of using standing MgO nanowires as templates is that these nanowires are well separated and do not shadow each other, and hence high-quality conformal coating can be readily achieved to yield core-shell nanowires. Figure 4(a) shows a SEM image of MgO/YBCO core-shell nanowires grown on a MgO(100) substrate using the PLD approach. Most of the nanowires are still normal to the substrate after the PLD process. EDS was performed to determine the ratio between the heavy elements, and a result of 1:2:3 for Y:Ba:Cu was obtained. The oxygen ratio was determined by comparing the lattice constants derived from the XRD pattern with the database [21]. Details of XRD analysis can be found in our previous publication [22]. These two techniques combined identified the coating layer as YBa₂Cu₃O_{6.66}. Furthermore, the core-shell nanowire structure was directly confirmed using low magnification transmission electron microscopy, as shown in figure 4(b). The MgO core can be seen to be 9 nm in diameter and coated with 15 nm thick YBCO conformally. Due to the difference in lattice spacing (MgO: $a_1 = 0.421\text{ nm}$ and YBCO: $a_2 = 0.382\text{ nm}$, $b = 0.388\text{ nm}$ and $c = 1.169\text{ nm}$) [21], overlapping of MgO crystals and YBCO crystals may form periodic beat-like structures and lead to the well known Moiré pattern in electron microscopy [23]. Moiré patterns (figure 4(c)) are observed in the inner region of core-shell nanowires, where overlapping MgO and YBCO lattices exist. In contrast, no such beating pattern was observed in the outer region (YBCO only) of the nanowire. The period of the Moiré pattern is determined to be $d_1 = 4.9\text{ nm}$, consistent with the value derived from the equation $d_1 = (a_1 \times b) \cos \omega / (a_1 - b)$, where a_1 is the (100) MgO spacing of 0.421 nm , b is (010) YBCO spacing of 0.388 nm and $\omega = 11.1^\circ$ is the tilt angle of Moiré fringe. From the angle ω , the tilt of (010) YBCO relative to (100) MgO is calculated as 0.9° [23]. This indicates that the YBCO nanowire is single crystalline with (010) being the axial direction. The epitaxial nature of the growth was further revealed by the HRTEM image shown in figure 4(d), where the lattice spacing of 2.75 Å between the (110) planes can be clearly resolved for the YBCO shell layer.

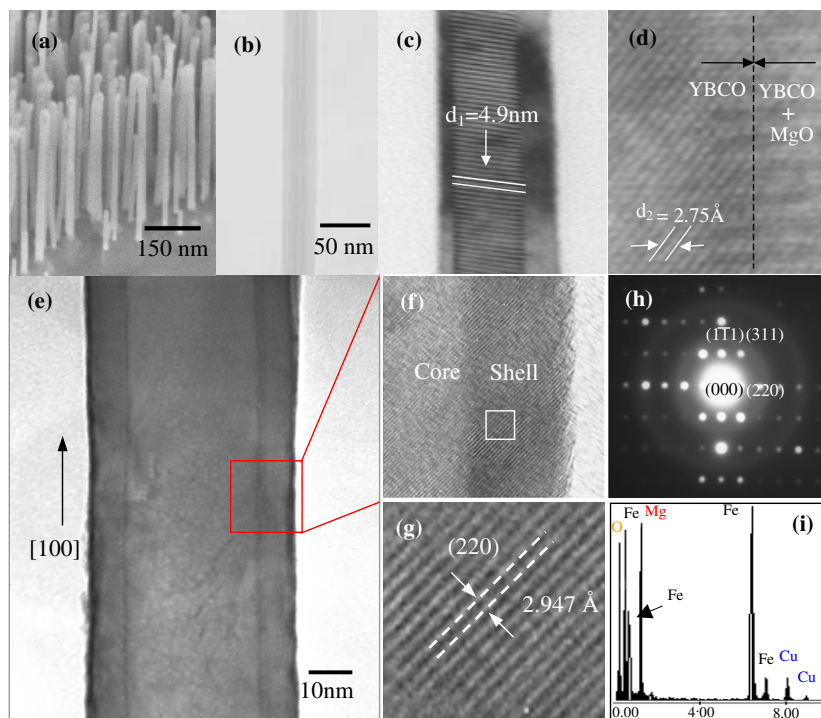


Figure 4. Characterization of MgO/YBCO and MgO/Fe₃O₄ nanowires. (a) SEM image of YBCO nanowires on a MgO(100) substrate after the PLD process. (b) Low magnification TEM image showing the MgO/YBCO core-shell structure. (c) TEM image of MgO/YBCO nanowire showing parallel Moiré patterns. (d) HRTEM image of the MgO/YBCO nanowire. (e) TEM image of a MgO/Fe₃O₄ core-shell nanowire. The boxed region has been enlarged in (f) to inspect the core-shell interface. (g) The boxed area in (f) was further enlarged to examine the lattice spacing in the shell region. (h) SAED pattern of the core-shell nanowire. (i) EDX data recorded with the nanowire, where signals from Mg, Fe and O were detected.

We have further applied this synthetic approach to produce MgO/Fe₃O₄ core-shell nanowires. Fe₃O₄ is an important material showing spin half metallic properties with a very high Curie temperature ($T_C = 850$ K) [24–26]. The synthesis was carried out via PLD to form MgO/Fe₃O₄ core-shell nanowires with the substrate temperature kept at 350 °C. The system was maintained at 7.5×10^{-2} Torr in a flow of Ar at 5 sccm opposite to the laser beam direction. The morphology of the nanowires has been investigated with TEM. Figure 4(e) shows a typical TEM image of the core-shell nanowire, indicating the uniform Fe₃O₄ coating on the MgO core. The diameter of the MgO core is ~25 nm and the thickness of the coated shell is ~7 nm. By looking at the interface of the core and shell in the HRTEM image (figure 4(f)), we can find that the interface between the MgO core and epitaxial magnetite shell appears relatively sharp. The lattice fringes are continuous from the core to the shell, confirming a perfect single crystal epitaxial growth of the Fe₃O₄ layer. By analysing the lattice fringes of the shell (shown in figure 4(g)), the lattice spacing between two planes is ~2.947 Å, corresponding to the distance of two (220) planes of Fe₃O₄. The angle between the interface of the core-shell and lattice fringe of the (220) plane is determined to be 45°. This tells us that the axial growth direction core is along [100], consistent with the growth direction of MgO nanowires. Figure 4(h) shows the [112] zone axis electron diffraction pattern of the core-shell nanowires, further confirming the single crystal nature. The corresponding nearest three spots in the figure can be indexed to (220), (111) and (311) planes of Fe₃O₄. EDX data (figure 4(i)) have also been

recorded with the nanowire, where signals from Mg, Fe and O were detected.

Our synthetic technique readily lends itself to other material systems, including LSMO, a CMR material [12], and PZT, a ferroelectric dielectric [13]. MgO nanowire templates were used for both materials and the technique details can be found in the previous publications [22, 27]. The core-shell nanowire structure was directly confirmed using TEM, as shown in figures 5(a) and (b). The MgO core can be seen to be 20 nm in diameter and coated with 10–15 nm thick LSMO. The coating is continuous but slightly nonuniform. More in-depth work is being carried out to achieve a uniform coating by adjusting the sample-target distance and rotating the sample during the deposition. In the inner core, periodic beat-like structures were observed, which correspond to well-known Moiré patterns due to the difference in lattice spacing of MgO ($d = 0.421$ nm) and LSMO ($d = 0.387$ nm) [23]. Moiré patterns were observed only in the inner region of core-shell nanowires, where electrons were diffracted by the stacked MgO and LSMO lattices. In contrast, no such beating pattern was observed in the outer region (LSMO only) of the nanowire. The electron diffraction pattern shown in figure 5(c) also confirms the epitaxial growth, as two sets of diffraction pattern were observed, corresponding to the MgO cubic lattice and the LSMO cubic perovskite lattice. TEM analysis of the MgO/PZT core-shell nanowires is shown in figures 5(d)–(f). The core-shell structure can be clearly seen in the TEM image in figure 5(d). Further TEM analysis also reveals [100] as the

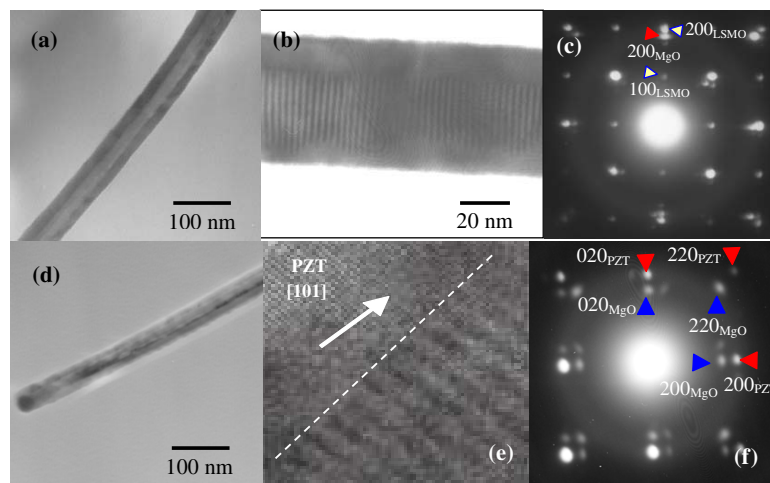


Figure 5. Characterization of MgO/LSMO and MgO/PZT nanowires. (a) Low magnification TEM image of as-grown MgO/LSMO nanowires on a MgO (100) substrate clearly showing core-shell structure. (b) TEM image of MgO/LSMO nanowire showing parallel Moiré patterns. (c) SAED pattern of a MgO/LSMO core-shell nanowire. (d) TEM image of a PZT nanowire. The catalyst can be seen at the end of the nanowire. (e) HRTEM image of the MgO/PZT core-shell nanowire at the sample tilt angle of 45°. (f) SAED pattern of a MgO/PZT nanowire. Light grey/red and dark grey/blue arrows indicate diffraction pattern from PZT and MgO, respectively.

axial direction for the PZT shell layer (figure 5(e)). Figure 5(f) reveals two sets of diffraction patterns for MgO and PZT and thus confirms the single crystal nature of our core-shell nanowires.

These high-quality core-shell nanowires provide unique opportunities to study a number of issues of fundamental importance, such as electronic transport, phase transition and anisotropic properties at nanoscale dimensions. Below we use our study on Fe_3O_4 and LSMO nanowires as examples [27, 28]. To fabricate devices based on individual nanowires, the nanowires were first sonicated off the substrate into isopropanol, and then dispersed onto a clean Si/SiO₂ substrate. E-beam lithography and thermo-evaporation were then used to pattern and deposit four electrodes to contact the nanowires. Ti/Au and Ag/Au were used as contact metals for Fe_3O_4 and LSMO core-shell nanowires, respectively. The transport studies have been carried out by measuring the four-probe resistance and magnetoresistance of both Fe_3O_4 and LSMO core-shell nanowire devices.

The SEM image shown in figure 6(a) is a perspective view of a typical device consisting of a 5 μm -long MgO/ Fe_3O_4 nanowire and four electrodes uniformly distributed on it. TEM studies performed with nanowires left in the suspension revealed the MgO diameter and the Fe_3O_4 shell thickness as being ~ 20 nm and ~ 8 nm respectively. We performed MR measurements with the MgO/ Fe_3O_4 core-shell nanowire, with the data shown in figure 6(b). The nanowire resistance was recorded at four different temperatures, while a perpendicular magnetic field was double-swept between $B = \pm 1.8$ T. MR of $\sim 1.25\%$ was achieved at $T = 290$ K and $B = 1.8$ T (corresponding to $H = 18$ kOe), and no saturation trend was observed within the scanned region. The obtained MR agrees with most previous studies on 2D Fe_3O_4 systems [29–31]. As has been pointed out, the MR, either in 2D epitaxial films or the 1D form in our case, is believed to arise from the spin-polarized transport across the anti-phase boundaries (APBs), where the magnetic moments of B-site cations were antiferromagnetic

(AF) coupled via a 180° superexchange interaction. A reduction in the resistivity is expected when the opposite moments at the APBs are slightly aligned by an applied magnetic field. In addition, the very strong AF coupling at the APBs induces very large saturation fields, which explains the absence of saturation in our measurements. The magnetoresistance ratio at $B = 1.8$ T was plotted versus T in the inset of figure 6(b), where the MR monotonically increased with the decreasing temperature. This is understandable, as decreasing the temperature improves the alignment in the magnetic domains, and also increases the degree of spin polarization near the Fermi level, and then contributes to an increase in the MR.

The transport studies on MgO/LSMO core-shell nanowires have also been carried out by measuring the four-probe resistance and MR of the nanowire devices. TEM studies performed with nanowires left in the suspension revealed the MgO diameter and the LSMO shell thickness as being ~ 20 and ~ 10 nm respectively. The LSMO resistivity is estimated to be $2.0 \times 10^{-4} \Omega \text{ m}$ at room temperature based on four-point probe measurements using a channel length of $\sim 1 \mu\text{m}$ (between the middle two electrodes) and a cross section of $\sim 1.57 \times 10^{-15} \text{ m}^2$ estimated from the shell geometry. Figure 6(c) shows the electrical resistance of a typical core-shell nanowire device under zero magnetic field as a function of temperature. The resistance displays a peak around 325 K, which corresponds to a transition of LSMO from an insulating state ($dR/dT < 0$) to a metallic state ($dR/dT > 0$). Figure 6(c) inset compares the R - T curves taken under zero and 1 T magnetic fields. One can clearly see that the device exhibited lower resistance in the 1 T magnetic field for temperatures between 250 and 295 K; however, for even lower temperatures ($T < 200$ K), the measured resistance exhibited little difference between zero and 1 T magnetic fields. This is consistent with the observation from epitaxial single-crystalline LSMO films, indicating the high quality of our LSMO epitaxial layer [32]. Figure 6(d) shows the MR measured at 295 K with a magnetic field up to

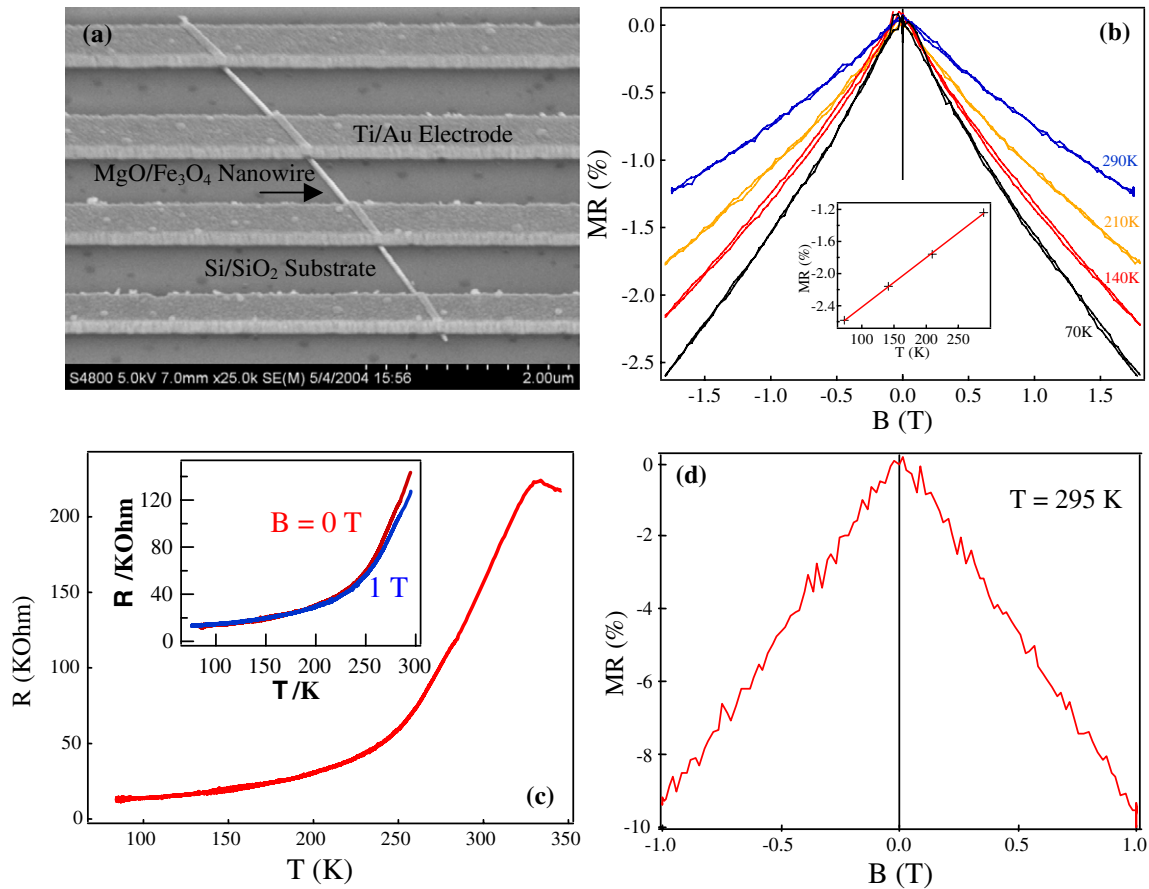


Figure 6. (a) SEM image shows a perspective view of the nanowire device, with four Ti/Au electrodes evenly distributed on the MgO/Fe₃O₄ core-shell nanowire. (b) Magnetoresistance of MgO/Fe₃O₄ core-shell nanowire device recorded at $T = 290$ K, 210 K, 140 K and 70 K, while a perpendicular magnetic field was double-swept between $B = \pm 1.8$ T. The magnetoresistance ratio at $B = 1.8$ T is also plotted as a function of temperature in the inset, which can be basically fitted into a straight line. (c) Resistance versus temperature data of a MgO/LSMO nanowire measured in 0 T magnetic field showing a transition temperature at 325 K. Inset: R versus T with 1 T and without magnetic field. (d) Magnetoresistance of MgO/LSMO core-shell nanowire measured at room temperature.

1 T, with MR defined as $[R(B) - R(0)]/R(B_{\max}) \times 100\%$, where $R(0)$, $R(B)$ and $R(B_{\max})$ are the device resistance at magnetic fields 0, B and B_{\max} (the maximum applied field), respectively. The resistance had its maximum value at zero field and was monotonically reduced by higher magnetic field. A magnetoresistance ratio can be determined to be -9.2% for this device at 1 T magnetic field. The observation of the metal-insulator transition above room temperature and the existence of colossal magnetoresistance in our MgO (20 nm)/LSMO (10 nm) core-shell nanowire systems is particularly noteworthy, as compared to the absence of metal-insulator transition previously observed for 26 nm LSMO films deposited on (001) MgO [33]. In contrast, the LSMO layer in our core-shell nanowires was only 10 nm in thickness, while the transition temperature reached 325 K, which is close to the bulk LSMO transition temperature [34]. In this study, four devices have been measured, and the transition temperatures were consistently around 325 K, indicating the high quality and reproducibility of our LSMO nanowires.

In addition to phase transition studies, LSMO nanowires also provided us with a unique opportunity to study anisotropic properties related to their high aspect ratio (>100). An electromagnet where the sample can be rotated 360° between

its pole pieces was used for this study at room temperature, with θ defined as the angle between the nanowire long axis and the magnetic field direction as shown in figure 7(a). The MR versus magnetic field at different angles was recorded. As shown in figure 7(b), all four curves taken at $\theta = 0^\circ$ (black square), 45° (blue circle with cross), 90° (green box), 135° (red circle with dot) displayed typical colossal magnetoresistance for magnetic fields between 0 and ± 0.9 T. With the magnetic field parallel to the nanowire, the MR had the highest value of -9.9% at ± 0.9 T. In contrast, the MR displayed its lowest value of -8.5% when the magnetic field H was applied normal to the nanowire. This corresponded to a 1.4% variation in MR at 0.9 T due to the shape-induced effect. This is more clearly revealed in figure 7(c), where the MR at 0.9 T is plotted versus the angle θ . This shape-induced magnetoresistance likely originates from the high aspect ratio of our nanowires, which gives us strong shape anisotropy. It is well known that for wire or rod like magnetic structures, the longitudinal direction is the easy magnetization direction, while the direction normal to the long axis represents the hard magnetization direction. Under the same magnetic field strength, a magnetic field parallel to the nanowire can therefore produce higher spin ordering than a field normal to the nanowire, which in turn leads to lower

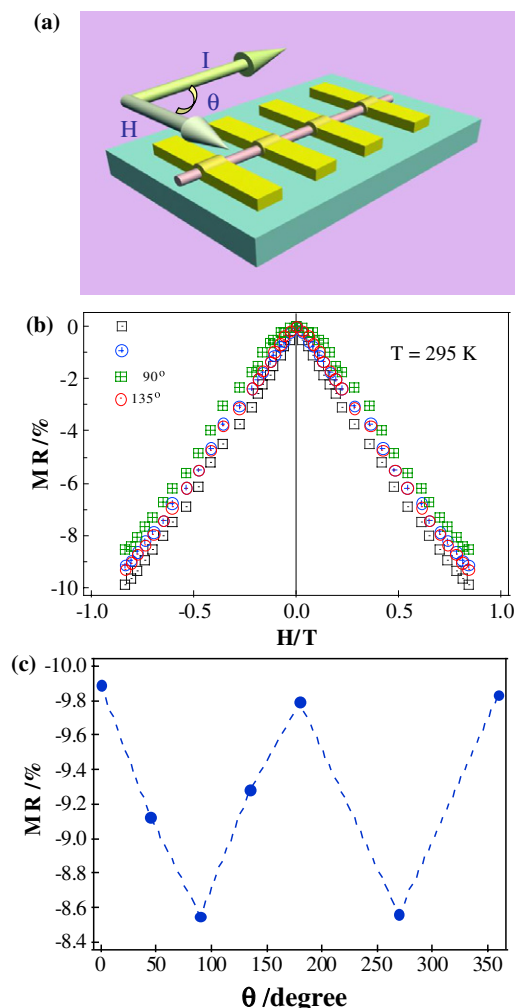


Figure 7. Room-temperature magnetoresistance measurements on a MgO/LSMO core-shell nanowire. (a) Schematic diagram of the measurement setup, where θ is defined as the angle between the nanowire long axis and the magnetic field direction. (b) Magnetoresistance for the magnetic field applied with $\theta = 0^\circ, 45^\circ, 90^\circ$ and 135° . (c) Plot of the magnetoresistance ratio versus the angle θ at 0.9 T magnetic field.

resistance when $\theta = 0^\circ, 180^\circ$, and 360° for the manganite nanowires [35, 36].

In summary we have presented a versatile synthetic approach to produce various high-quality, single crystalline transition metal oxide nanowires. The electronic transport and magnetoresistance properties have been investigated with Fe_3O_4 and LSMO nanowires. Fe_3O_4 nanowire exhibited a room-temperature magnetoresistance of 1.2% under a magnetic field of $B = 1.8\text{ T}$. $\text{La}_{0.67}\text{Sr}_{0.33}\text{MnO}_3$ nanowire showed a remarkable metal-insulator transition at 325 K , accompanied by room-temperature colossal magnetoresistance $\sim 10\%$ under a 1 T magnetic field. More interestingly, shape-induced magnetoresistance was observed at room temperature. Our technique can be easily generalized to synthesize a wide variety of novel core-shell nanowires, which may find important applications for spintronics and magnetic data storage.

Acknowledgments

We thank Professor Edward Goo for helpful discussions and USC Microscope Center for the use of their facilities. We also thank Dr Jinping Zhang for the help with the HRTEM. We acknowledge support of this work by a National Science Foundation CAREER Award and Defense Advanced Research Projects Agency.

References

- [1] Lieber C M 2003 Nanoscale science and technology: building a big future from small things *MRS Bull.* **28** 486–91
- [2] Wang X D and Wang Z L 2004 *Nanoengineering of Structural, Functional and Smart Materials* (CRC Press) chapter 4
- [3] Pauzauskie P and Yang P 2006 Nanowire photonics *Mater. Today* **9** 36–45
- [4] Patolsky F, Zheng G and Lieber C M 2006 Nanowire-based biosensors *Anal. Chem.* **78** 4260–9
- [5] Xia Y and Yang P 2003 Nanowires *Adv. Mater.* **15** 353–89 (Special issue)
- [6] Wagner R S and Ellis W C 1964 *Appl. Phys. Lett.* **4** 889–90
- [7] Trentler T J, Hickman K M, Geol S C, Viano A M, Gibbons P C and Buhro W E 1995 *Science* **270** 1791–4
- [8] Heath J R and LeGoues F K 1993 *Chem. Phys. Lett.* **208** 263–8
- [9] Xia Y, Yang P, Sun Y, Wu Y, Mayers B, Gates B, Yin Y, Kim F and Yan H 2003 *Adv. Mater.* **15** 353–89
- [10] Urban J J, Yun W S, Gu Q and Park H 2002 *J. Am. Chem. Soc.* **124** 1186–7
- [11] He R, Law M, Fan R, Kim F and Yang P 2002 *Nano Lett.* **2** 1109–12
- [12] Jiang J, Henry L L, Gnanasekar K I, Chen C and Meletis E I 2004 *Nano Lett.* **4** 741–5
- [13] Dai P, Mook H A, Aeppli G, Hayden S M and Doğan F 2000 *Nature* **406** 965–8
- [14] Prinz G A 1999 *Science* **282** 1660–3
- [15] Gregg J F, Petej I, Jouguelet E and Dennis C J 2002 *J. Phys. D: Appl. Phys.* **35** R121–55
- [16] Moreo A, Yunoki S and Dagotto E 1999 *Science* **283** 2034–40
- [17] Fäth M, Freisem S, Menovsky A A, Tomioka Y, Aarts J and Mydosh J A 1999 *Science* **285** 1540–2
- [18] Tybell T, Paruch P, Giamarchi T and Triscone J-M 2002 *Phys. Rev. Lett.* **89** 097601–4
- [19] Ahn C H, Rabe K M and Triscone J-M 2004 *Science* **303** 488–91
- [20] Kwon C et al 1996 *Superlatt. Microstruct.* **19** 169–81
- [21] Hu J, Odom T W and Lieber C M 1999 *Acc. Chem. Res.* **32** 435–45
- [22] Lei B, Li C, Zhang D, Han S and Zhou C 2005 *J. Phys. Chem. B* **109** 18799–803
- [23] Henry N F M and Lonsdale K 1952 *International Tables for X-ray Crystallography* vol I (England: The Kynoch Press)
- [24] Pan Z W, Dai Z R and Wang Z L 2001 *Science* **291** 1947–9
- [25] Liu Y, Zadorozhny Y, Rosario M M, Rock B Y, Carrigan P T and Wang H 2001 *Science* **294** 2332–4
- [26] Wu Y, Yan H, Huang M, Messer B, Song J and Yang P 2002 *Chem. Eur. J.* **8** 1261–8
- [27] PCPDFWIN 1999 Version 2.02 *Int. Center for Diffraction Data* (ICDD: Newtown Square)
- [28] Han S, Li C, Liu Z, Lei B, Zhang D, Jin W, Liu X, Tang T and Zhou C 2004 *Nano. Lett.* **4** 1241–6
- [29] Hirsch P 1977 *Electron Microscopy of Thin Crystals* (Malabar, FL: Krieger)
- [30] de Groot R A, Mueller F M, van Engen P G and Buschow K H J 1983 *Phys. Rev. Lett.* **50** 2024–7
- [31] Zhang Z and Satpathy S 1991 *Phys. Rev. B* **44** 13319–31

- [26] Yanase A and Siratori K 1984 *J. Phys. Soc. Japan* **53** 312–7
- [27] Li C, Lei B, Luo Z, Han S, Liu Z, Zhang D and Zhou C 2005 *Adv. Mater.* **17** 1548–53
- [28] Zhang D, Liu Z, Han S, Li C, Lei B, Stewart M P, Tour J M and Zhou C 2004 *Nano Lett.* **4** 2151–5
- [29] Sena S P, Lindley R A, Blythe H J, Sauer C, Al-Kafarji M and Gehring G A 1997 *J. Magn. Magn. Mater.* **176** 111–26
- [30] Zhang Z Z, Cardoso S, Freitas P P, Batlle X, Wei P, Barradas N and Soares J C 2001 *J. Appl. Phys.* **89** 6665–7
- [31] Liu H, Jiang E Y, Bai H L, Zheng R K, Zhang Wei H L and Zhang X X 2003 *Appl. Phys. Lett.* **83** 3531–3
- [32] Gupta A, Gong G Q, Xiao G, Duncombe P R, Lecoeur P, Trouilloud P, Wang Y Y, Dravid V P and Sun J Z 1996 *Phys. Rev. B* **54** R15629–32
- [33] Steren L B, Sirena M and Guimpel J 2000 *J. Magn. Magn. Mater.* **211** 28–34
- [34] Tokura Y, Tomioka Y, Kuwahara H, Asamitsu A, Morimoto Y and Kasai M 1996 *J. Appl. Phys.* **79** 5288–91
- [35] Jaccard Y, Guittienne P, Kelly D, Wegrowe J-E and Ansermet J P 2000 *Phys. Rev. B* **62** 1141–7
- [36] Wegrowe J-E, Kelly D, Franck A, Gilbert S E and Anserme J-P 1999 *Phys. Rev. Lett.* **82** 3681–4